

Hyperpolarized ^3He Gas Production and MR Imaging of the Lung

JASON C. LEAWOODS,¹ DMITRIY A. YABLONSKIY,^{1,2} BRIAN SAAM,³
DAVID S. GIERADA,² MARK S. CONRADI^{1,2}

¹*Department of Physics-1105, Washington University, St. Louis, Missouri 63130*

²*Department of Radiology-8131, Washington University, St. Louis, Missouri 63130*

³*Department of Physics, University of Utah, Salt Lake City, Utah 84112*

ABSTRACT: Optical polarization of ^3He generates large nuclear spin magnetizations, allowing MR imaging of the gas spaces of human and animal lungs despite the low number density of spins in the gas. The atomic physics of optical pumping and spin exchange is explained; the hardware for polarizing, transporting, and imaging is detailed. Pulse sequences for optimum use of the nonrenewable magnetization require a different imaging strategy than traditional proton MRI. Examples are discussed for static lung images, diffusion images for characterization of the local alveolar structure, and high temporal resolution images. © 2001 John Wiley & Sons, Inc. Concepts Magn Reson 13: 277–293 2001

KEY WORDS: hyperpolarized; NMR; MRI

INTRODUCTION

Most MRI of humans and animals uses proton NMR (1, 2). This is primarily because, to an NMR spectrometer, we are simply bags of dirty water with a very high density of hydrogen nuclei (100 mol/L) with sufficiently long T_2 (narrow resonance line). As gases at 1 atm have densities (and nuclear spin densities) about 1/1000 that of liquid water, there are simply too few spins to allow

imaging of gas in the lung space using ordinary NMR techniques.

Beginning nearly 40 years ago the technique of optical pumping (generating alignment of spins by transferring angular momentum to the spins from polarized light) has been studied and developed (3–6). Recently, the field has expanded rapidly with the advent of inexpensive, high-power diode laser arrays (7). Liter quantities of ^3He or ^{129}Xe can now be routinely produced in a matter of hours, with absolute nuclear polarizations of approximately 40%. Compared to Boltzmann equilibrium (the source of nuclear spin signal for nearly all NMR and MRI ever done) at typical values of 300 K and 1.5 Tesla, these optically pumped gases have polarizations greater by a factor of order 100,000—hence the name hyperpolarization. The increased polarization more than overcomes the inherently low spin density of gases.

Received 17 April 2001; revised 22 May 2001; accepted 24 May 2001.

Correspondence to: Jason C. Leawoods; E-mail: leawoods@hbar.wustl.edu.

In our research we have focused on ^3He and will do so also in this paper.

We have been active in MR imaging of human lungs with hyperpolarized ^3He , both in healthy volunteers and in patients with lung disorders (8, 9). Because the gas is imaged, as opposed to the hydrogen nuclei in lung tissue, we can depict the flow of gas into and out of the lung. Multi-slice ^3He MR images of the entire lung have been recorded as fast as every 0.6 seconds, making this technique the only method capable of recording ventilatory dynamics on a time scale shorter than the breathing period.

When we began this effort, we had to construct the required apparatus for polarizing the ^3He gas. The present paper describes the hardware as well as the physics of the polarization process. The techniques for transportation of the hyperpolarized gas to the imager and delivery of the gas to human subjects are detailed. We also discuss the different imaging strategy dictated by the nonrenewable nature of the hyperpolarized nuclear spin magnetization. The aim of the article is to allow the reader to understand the techniques and to increase the number of research groups involved in polarized-gas NMR and MRI. We note three earlier articles in *Concepts* on hyperpolarized nuclear spins which may be of interest to the reader (10–12).

THE POLARIZATION PROCESS

Boltzmann Polarization

Before considering laser-polarized nuclear spins we begin by treating Boltzmann equilibrium, the source of spin magnetization for virtually all NMR and MRI experiments (13). The case of a nuclear spin one-half is reviewed in Fig. 1. The Zeeman energy splitting between the two levels is hf , where f is the MR frequency and h is Planck's constant. This splitting is, in almost all cases, a tiny fraction of the thermal energy kT ($hf \ll kT$), leading to thermal equilibrium populations that are almost equal:

$$\frac{n_{\downarrow}}{n_{\uparrow}} = e^{-hf/kT} \approx 1 - \frac{hf}{kT} \quad [1]$$

where n_{\uparrow} and n_{\downarrow} represent the numbers of spins aligned and anti-aligned with the magnetic field.

The net spin magnetization arises only from the excess spins in the lower energy state; the other spins' magnetic moments cancel. Thus, the fraction of excess spins is the absolute polarization P ,

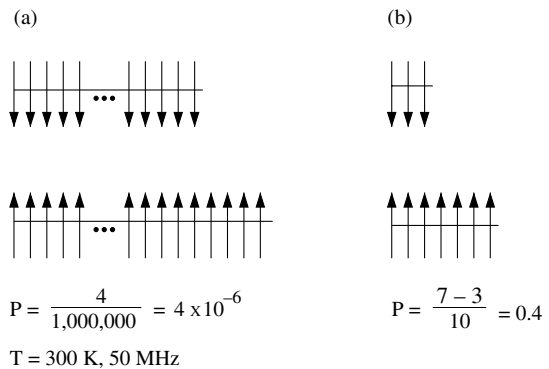


Figure 1 Energy levels for a nuclear spin one-half, showing relative populations (A) in thermal equilibrium at 300 K and 50 MHz. At these typical conditions, only four spins out of 10^6 are excess in the low-energy state. The case of laser-polarized spins (B) corresponds typically to four excess spins in the lower state out of every 10 spins, or $P = 0.4$.

where

$$P = \frac{n_{\uparrow} - n_{\downarrow}}{n_{\uparrow} + n_{\downarrow}}. \quad [2]$$

The value $P = 1$ corresponds to all spins being in the lower state, and $P = 0$ is the case of equal populations (saturation or infinite spin temperature).

In thermal equilibrium for $hf \ll kT$, Eq. [1] yields

$$P = \frac{hf}{2kT} \quad [3]$$

For typical proton MRI values ($f = 50$ MHz and $T = 300$ K), P will be 4×10^{-6} ; MR signals will arise from only four spins out of every one million in the sample, as shown in Fig. 1(A). The extremely small value of polarization P in thermal equilibrium is a primary reason for the notorious insensitivity of NMR and MRI compared to other (e.g., optical) spectroscopies. The techniques described here for hyperpolarizing noble gases yield a nuclear polarization of 40% or more, as presented in Fig. 1(B). Such high polarizations exceed that attainable in thermal equilibrium by a factor of order 10^5 and deliver correspondingly stronger MR signals (10^5 in voltage units or 100 dB).

Depopulation Optical Pumping

There are currently two techniques for producing hyperpolarized gases. The first involves direct optical excitation of metastable atoms produced in an electric discharge (6, 14); this method only

works for ^3He . Advantages of this method, often called metastability pumping, are that it requires no alkali metal as an intermediary to transfer the angular momentum from photons to nuclear spins and the intrinsically high polarization rate. Disadvantages include the unavailability of suitable diode lasers at the correct wavelength and the necessity of mechanically compressing the hyperpolarized gas from 1 Torr up to 1 atmosphere or greater without destroying the polarization. We note that an efficient and compact compressor has been described recently for this approach (15).

The second method is optical pumping of an alkali-metal vapor followed by spin exchange between the alkali metal and the noble gas (16, 17). This involves the consecutive transfer of angular momentum from circularly polarized light to the electron spins of the alkali atoms and then to the nuclear spins of the noble gas. This works for all noble-gas nuclear spins but works best for spins one-half because of their longer T_1 values; the only stable spin one-half noble gases are ^3He and ^{129}Xe . The following discussion will be phrased in terms specific to our application: optical pumping of Rb and subsequent spin exchange to ^3He nuclei.

Optical pumping of Rb is depicted in Fig. 2, where the $5s_{1/2}$ electronic ground state and $5p_{1/2}$ first excited state are shown, with transitions between the states driven by resonant photons at 794.7 nm. The spectroscopic notation refers to the single active electron outside the filled, core shells: $n = 5$ is the principal quantum number, s and p refer to orbital angular momentum $\ell = 0$ and 1, respectively, and the subscript 1/2 implies that the total angular momentum $j = 1/2$ (the sum of spin and orbital angular momenta). The $5p_{3/2}$ level, inactive in the optical pumping process, is slightly higher in energy than $5p_{1/2}$ because of spin-orbit splitting. The weak, applied magnetic field (typically 10–30 Gauss) breaks each state into two sublevels characterized by $m_j = -1/2$ or $+1/2$. In the $5s_{1/2}$ ground state, $m_j = \pm 1/2$ is simply electron spin up or down, since there is no orbital contribution to j .

The purpose of the magnetic field is to impose a spin quantization axis along the direction of light propagation (and angular momentum). The crucial aspect is the magnetic selection rule for the transitions from $5s_{1/2}$ to $5p_{1/2}$; the small Zeeman splitting is trivial and is not involved in the physics of the process. For left-handed circularly polarized light ($\sigma+$), for which each photon carries one quantum of angular momentum parallel to the

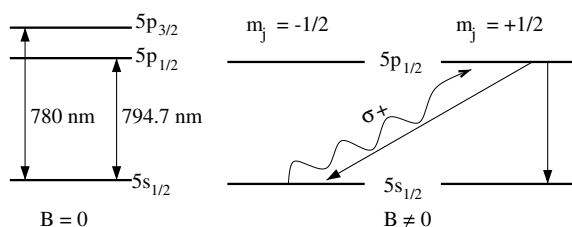


Figure 2 Rb electron energy levels and transitions involved in optical pumping. For $B = 0$ (at left) the lowest three energy levels and optical transitions at 794.7 and 780 nm are shown. The lowest two energy levels are also depicted for $B \neq 0$ (at right): left-handed, circularly polarized light ($\sigma+$) can only excite the transition shown (wavy arrow), because of the magnetic selection rule $\Delta m_j = +1$. Subsequent transitions to the ground state (straight arrows), combined with continual optical pumping, cause the $m_j = -1/2$ ground state to be depopulated, leaving essentially all the population in the $m_j = +1/2$ ground level.

propagation axis of the light (chosen to be parallel to the magnetic field), $\Delta m_j = +1$. This magnetic selection rule is simply a statement of the conservation of the component of angular momentum along the propagation axis for the photon–atom system. The curvy arrow $\sigma+$ in Fig. 2 shows the only allowed transition; all others would be a violation of the magnetic selection rule.

Once excited to the $5p_{1/2}$, $m_j = +1/2$ state, the atom will return to either of the two ground sublevels with approximately equal probabilities. If the atom returns to the $m_j = +1/2$ ground level, the net effect has been to move one ground-state atom from $m_j = -1/2$ to $+1/2$. If the atom de-excites by returning to $m_j = -1/2$, there is no net effect and the atom is again available for optical excitation. Continuous optical irradiation will depopulate the $5s_{1/2}$, $m_j = -1/2$ (“spin-down”) state, leading to all Rb electron spins being $5s_{1/2}$, $m_j = +1/2$ (“spin-up”). Hence, this technique is known as depopulation optical pumping. With all Rb spins up, no further optical transitions can occur, according to the $\Delta m_j = +1$ selection rule. To repolarize the electrons that relax from spin up to spin down via ground-state electron T_1 processes (mainly from electron–electron and electron–rotation interactions, of order 1 ms under our conditions), one must supply approximately two photons per Rb atom per Rb T_1 time constant. This criterion determines the optical power required to support the process (18).

During the short time T_1 that electrons remain polarized, they will diffuse a distance approximately equal to $\sqrt{(2Dt)}$, where D is the Rb

diffusivity. Taking an estimated value of $D = 10^{-2} \text{ cm}^2/\text{s}$ and $t = T_1 = 10^{-3} \text{ s}$, the atoms will diffuse only about 0.1 mm before depolarizing. Thus, any dark regions in the optical illumination of the polarizing cell will have low or zero Rb polarization; Rb diffusion is inadequate to bring about spatial averaging.

If de-excitation from the $5p_{1/2}$ excited state is allowed to occur by photon emission, those photons will generally have a different polarization and propagation direction than the incident light. Since the Rb vapor is optically thick, photons of the wrong polarization are always reabsorbed. Such a situation of multiple absorption and re-emission of photons is known as radiation trapping and is to be avoided because it effectively depolarizes the light field. Collisional de-excitation is promoted by a small concentration ($\approx 1\%$) of N_2 buffer gas, which carries away much of the 1.5 eV excitation energy as rotations and vibrations.

The $5p_{3/2}$ level resides only about 0.03 eV (comparable to kT) above $5p_{1/2}$; thus, occasionally a $5p_{1/2}$ excited state atom is further excited to $5p_{3/2}$ by thermal energy delivered during a collision. A subsequent transition to the ground state can emit a photon at 780 nm. With the use of a highly selective optical filter, this fluorescence may be separated from the much more intense 794.7 nm scattered laser light. The spatial variation of the fluorescence is a useful diagnostic tool for determining the uniformity and efficiency of the optical excitation.

Spin Exchange

The Rb electronic polarization will be transferred to the nuclei of ^3He by collisional overlap of the electronic and nuclear wave functions (16, 17). During a collision between Rb and ^3He atoms, the Rb electronic wave function overlaps the ^3He nucleus, resulting in a Fermi-contact interaction described by a Hamiltonian $\mathcal{H} = a(r) \mathbf{I} \cdot \mathbf{S}$. Here, \mathbf{I} represents the ^3He nuclear spin operator and \mathbf{S} represents the Rb electronic spin operator. The function $a(r)$ expresses the wave function overlap onto the ^3He nucleus and is a strong, exponential function of Rb- ^3He distance, becoming zero whenever the atoms are well separated. This Hamiltonian contains terms I^+S^- and I^-S^+ , corresponding to mutual spin-flips that transfer the angular momentum from the Rb electron to the ^3He nucleus and vice-versa (flip-flop and flop-flip) (13). If the only source of nuclear-spin transitions were interactions with the Rb electron spins

(i.e., if in the absence of Rb, the ^3He T_1 were infinite), 100% electron spin polarization would lead to 100% nuclear spin polarization.

The spin exchange process occurs at a rate γ_{se} , which is linearly proportional to the density of Rb vapor. Essentially, a tiny fraction of Rb- ^3He collisions are successful in reorienting a ^3He nuclear spin; thus the Rb density, collision rate, and spin exchange rate are all linearly proportional. The Rb vapor density is easily regulated by the temperature of the cell, with an excess of liquid Rb in equilibrium with the vapor. The Rb vapor pressure is a strong function of temperature (in dynes/cm², $\log_{10} p = 10.55 - 4132/T$) (19). We work at $[\text{Rb}] = 1.47 \times 10^{14}/\text{cc}$ (157 °C) and γ_{se} is found experimentally to be $(8 \text{ h})^{-1}$. It therefore takes about 24 hours to build up nearly full ^3He polarization. Our high measured value of γ_{se} compared to Baranga, et al. (18) implies that laser heating may increase the cell temperature significantly.

In competition with the polarizing process, the intrinsic nuclear-spin T_1 processes tend to destroy the nuclear polarization. The intrinsic T_1 of ^3He (due to He-He collisions) is approximately 80 h at 10 atm (20). In the relaxation of monatomic gases (21), the dipolar spin-spin interaction is only present during the brief collisions; consequently, the relaxation rate T_1^{-1} is proportional to the rate of collisions and hence density and pressure. The principal source of relaxation, however, is usually collisions with, or adsorption to, the walls of the container. The polarizing process for ^3He is exceedingly slow; thus, finding the right container walls or chemically treating the walls of a ^3He polarizing vessel to yield a long T_1 is vital to producing large nuclear spin polarizations.

The rise of ^3He polarization P during the pumping process follows:

$$\frac{dP}{dt} = \gamma_{\text{se}}(P_{\text{Rb}} - P) - T_1^{-1}P \quad [4]$$

where the first term on the right represents spin exchange with Rb and the second term describes leakage of the magnetization through ^3He T_1 processes. P_{Rb} represents the Rb electronic polarization. For zero polarization at time $t = 0$, the usual case,

$$P = \frac{P_{\text{Rb}}\gamma_{\text{se}}}{(\gamma_{\text{se}} + T_1^{-1})} (1 - e^{-(\gamma_{\text{se}} + T_1^{-1})t}) \quad [5]$$

At short times the polarization from Eq. (5) is $P = P_{\text{Rb}}\gamma_{\text{se}}t$; this behavior appears in Fig. 3, where the initial slope is independent of the ^3He T_1 .

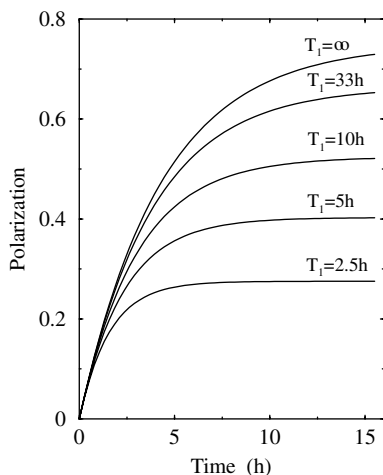


Figure 3 Increase of polarization with time for several values of ^3He relaxation time constant T_1 , with a fixed spin exchange rate γ_{se} of $(5 \text{ h})^{-1}$ and a fixed Rb polarization of 0.75. For $T_1 \gg (\gamma_{\text{se}})^{-1}$ the ^3He polarization nearly attains its full value of 0.75.

For a short T_1 the steady-state limit is obtained in a shorter time, but the polarization is reduced. The long-time limit is then

$$P = \frac{P_{\text{Rb}}\gamma_{\text{se}}}{\gamma_{\text{se}} + T_1^{-1}} \quad [6]$$

Clearly, P approaches the Rb polarization when γ_{se} is much larger than the ^3He T_1^{-1} . Because γ_{se} is proportional to Rb density, it can easily be increased by heating the cell; for fixed P_{Rb} this will increase the final ^3He polarization and reduce the time to develop full polarization. As the number of Rb atoms is increased, however, the Rb polarization will eventually decrease because of the limited flux of photons, as discussed above. Optimum polarizing conditions use the largest Rb density (highest cell temperature) that can be maintained in high polarization by the available light source.

Overall, the process of polarizing ^3He resembles filling a bucket with an eyedropper; the process is slow because γ_{se} is so small. With sufficient patience the bucket will fill eventually, provided there are no leaks. Here the leaks represent ^3He T_1 processes; large polarizations can only be produced in cells with long T_1 's.

The above discussion assumed pumping with left-handed circularly polarized light. With right-handed light the Rb polarization would be inverted and the resulting ^3He polarization would invert as well, resulting in NMR signals of opposite (emissive) phase. While it is occasionally

useful to verify that the NMR signal originates from the polarized gas by switching the helicity of the light, we avoid this situation. Large emissive spin magnetizations can behave as a MASER when placed in high-Q tuned circuits, leading to rapid polarization losses (21–23). Such effects are demonstrations of “radiation damping”; the emissive phase turns the damping into growth, leading to self-oscillation.

An alternate view of spin exchange is as an example of the Overhauser effect (13). The Rb electron and ^3He nucleus are coupled together in relaxation via their fluctuating Fermi contact interaction. In the usual application of the Overhauser effect, electron spins are driven from equilibrium by a saturation or inversion; here the electron spins are prepared far from Boltzmann equilibrium by optical pumping.

POLARIZER HARDWARE

We constructed our own hardware for polarizing both ^3He and ^{129}Xe . At one time a turnkey system was available from Magnetic Imaging Technologies, Inc. (24). Our philosophy has been to employ commercial components and to include as much diagnostic equipment as possible. Even though the system is reliable, the diagnostic measurements are invaluable for isolating the inevitable changes that occur in this multi-step, complex process. For example, we have suffered decreased laser output, increased laser linewidth, shortened T_1 of the pumping cell, impure gas, and poor optical collimation, among other problems. However, our two polarizers now perform with very little attention. The polarizer hardware is sketched in Fig. 4; we describe each component below.

Technology for semiconductor lasers has much improved in the last decade, and high power laser diode arrays are now available at reasonable prices. Diode lasers have almost completely displaced the much more expensive and inefficient Ti-sapphire/Ar-ion driver packages used previously. We employ a linear array of 10 diodes with approximately 50% efficiency and 40 W of output in the near infrared at 794.7 nm (25). This is a bare laser assembly which we mount to an aluminum, water-cooled heat sink through an indium foil thermal-contact pad and to which is supplied 38 A dc at 2 V. The attraction of this approach is its low cost (<\$5000); for more money one can obtain a complete laser system with a power inlet plug and an optical-fiber output. The laser has a

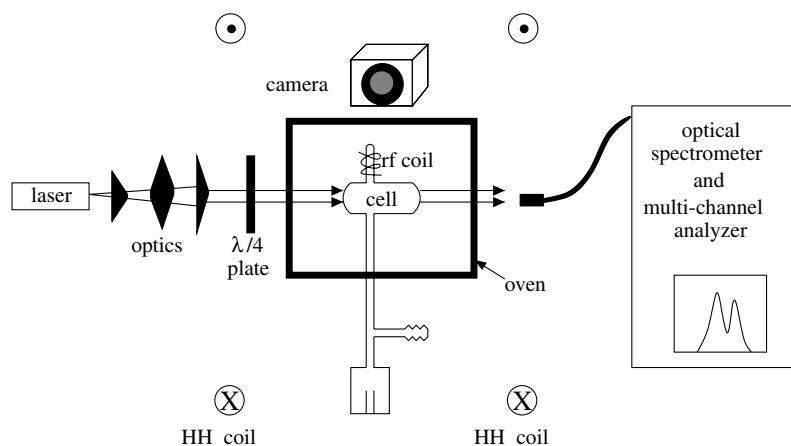


Figure 4 Apparatus for polarizing ^3He . The essential components are the laser and optics, the glass polarizing cell with ^3He and Rb, and the Helmholtz pair. The remaining pieces are diagnostic devices for monitoring the process.

rapid angular divergence in one direction, which is collimated by converging cylindrical lenses near the laser. Then the linearly polarized light from the laser is converted to be circularly polarized via a mica quarter-wave plate (26). By rotating the plate so that its principal axis is plus or minus 45° to the linear polarization axis of the light, one determines whether the circular polarization is right- or left-handed.

A disadvantage of current laser diode arrays is their excessive linewidth; our units have linewidths between 1.5 and 2.0 nm. It is thus important to pressure-broaden the Rb absorption line in order to use more of the laser photons (27). Our practice is to fill the glass polarizing cells to 10 atm at room temperature; we estimate that $1/3$ to $1/2$ of the photons are absorbed by the Rb. There has been recent progress in narrowing the laser line by wavelength-selective optical feedback employing diffraction gratings (28–30). These promise to deliver higher polarizations with smaller laser power. This is especially true for ^{129}Xe , where pressure-broadening is less successful.

The wavelength of diode lasers is controlled by regulating their temperature, so it is necessary to control the heat-sink temperature to within 1°C . We are careful to purchase laser diodes that tune to 794.7 nm at a reasonable temperature (operation at low temperatures leads to water condensation, which can damage the laser diode). N_2 purge gas around the laser aids in protecting it against condensation. We use a self-contained, chilled water system (31) but note that flowing tap water with a temperature regulator would be an inexpensive alternative. The small heat produced in our laser (only 40 W) makes water cooling

overkill; a more modern approach would be an air-cooled thermoelectric module.

The dc power to the laser is provided by a commercial, current-regulated supply. In one of our polarizers the laser is protected from excessive current faults by published circuitry (32). In the more recent polarizer, protection is provided by the SCR overvoltage protection internal to the power supply. The resistance of the wiring between the laser and the supply is chosen to be large enough that the voltage at the supply rises appreciably with the current (the voltage across the diode itself is virtually independent of current). The laser is further protected from low coolant flow and over-temperature by a simple interlock (32), with normally closed sensor switches wired in series.

Helmholtz coils provide a field of approximately 30 Gauss and are driven with 22 V at 4 A. The coils are wound in circular channels, either rolled and welded in a machine shop or purchased as aluminum bicycle rims. The 20-inch diameter and 10-inch spacing result in good field homogeneity, both for NMR polarization measurements and to reduce spin relaxation. As spins diffuse through a magnetic field gradient G , the field direction varies (Maxwell's equation $\nabla \cdot \mathbf{B} = 0$ prohibits an inhomogeneous field in a fixed direction). If the diffusion is sufficiently fast, the magnetization will be unable to completely adiabatically follow the changing magnetic field direction. Thus, diffusion at rate D through a gradient results in a contribution to the relaxation rate as $T_1^{-1} \cong D(G/B)^2$; a highly homogeneous magnetic field avoids this effect (4, 5, 33).

The ^3He gas is polarized in a sausage-shaped glass cell of about 7 cm length and 3.5 cm outer

diameter. The 50 cm^3 vessel is filled with 10 atm of ^3He with 1% N_2 and 100–300 mg of Rb. A glass valve is located outside of the oven to keep its o-rings cool and is connected to the cell by a long glass capillary tube. NMR measurements of the ^3He polarization in the 30 Gauss field use a solenoidal rf coil that slips on the short, 6 mm diameter tube extending from the cell. The coil form can be made of any high-temperature plastic, including Teflon.

The polarizing cell rests inside a home-built oven, approximately 15 cm on a side, made of aluminum and insulated with ceramic fiberboard. The top and front are removable for access to the cell. Air is supplied at 200 SCFH (5400 L/h) through a 1000 Watt (maximum) resistance heater. We take care to remove particulates, oil, and water from the compressed air supply. A platinum resistance thermometer sensor and a commercial temperature regulator close the feedback loop. Small glass windows allow the light into the cell and out to the diagnostic monitoring equipment.

The fluorescence from the Rb $5p_{3/2}$ level is monitored by a small video camera of the \$100 variety used for surveillance. A narrow-bandpass interference filter centered at 780 nm is used to exclude scattered laser light at 794.7 nm. If the fluorescence pattern does not uniformly extend to the rear of the cell, this suggests too high a Rb density, inadequate laser power, or insufficient pressure broadening. The spectrum of light transmitted through the cell is monitored to allow the laser wavelength to be centered on the Rb absorption peak. Since the Rb absorption is narrower than the laser, the transmitted spectrum is that of the laser, with a deep, wide notch in the center from the Rb. Light exiting the oven is collected by a plastic rod serving as an optical fiber and is delivered to a grating spectrometer. The dispersed light is detected by an optical multi-channel analyzer (34), with output displayed on a dedicated oscilloscope. We have also used an optical spectrometer on a PC circuit card (35).

The optics should be adjusted to uniformly illuminate the polarizing cell without much waste. We use additional video cameras to visualize the infrared laser beam by means of a low reflectivity beam stop (black anodized aluminum). Occasionally we monitor the total output power of the diode laser; a 1/2 kg block of aluminum, painted black to absorb light, is fitted with a thermocouple. The temperature rise in 30 s (typically $20\text{ }^\circ\text{C}$) is measured to calculate the power.

In the near infrared 40 W is potentially dangerous; it can burn the skin and explode the eye. The divergent nature of the light from the laser and the large diameter of the collimated beam (3.5 cm) reduce the hazard. Adequate laser-safety eyewear, however, is a must (36, 37). Black painted or anodized surfaces will reduce reflections. We employ warning signs and limited access to the laser room. A power-off switch outside the room allows emergency entry.

GLASS POLARIZING CELLS

Basic Characteristics

Widely varying, often anecdotal recipes for glass type, surface coating, and overall fabrication protocol have lent a folk-art character to the fabrication of useful polarization cells. This is directly related to an enduring problem in HP-gas research: the noble-gas nuclear relaxation time T_1 , which limits both the final gas polarization during its production and the subsequent time for storage and transport (e.g., to an MRI scanner). There are three important sources of spin-lattice relaxation under optical pumping conditions: (1) ^3He – ^3He collisions (bulk relaxation), (2) diffusion through magnetic-field gradients (5, 33), and (3) collisions with the container walls. The Helmholtz coils we use are sufficient to render gradient relaxation negligible at our pressures. The bulk relaxation time is inversely proportional to gas density and is about 80 h for 10 atm of ^3He at room temperature (20). Thus, wall relaxation not only dominates T_1 in many cases, but for most surfaces it is poorly understood.

For the application of HP ^3He to MRI, polarization cells should be valved, able to withstand ≥ 10 atm pressure in a volume $\geq 40\text{ cm}^3$, and have a stable $T_1 \geq 30$ h. Glass is almost always used, as it is transparent to the laser light and alkali-metal resistant. If T_1 is about five times greater than a typical spin-exchange time constant, the theoretical maximum ^3He polarization $\geq 85\%$ results (assuming 100% Rb polarization); see Eq. [6]. Such a cell is capable of producing ≥ 0.4 STP liters of HP- ^3He in 10–15 h of optical pumping with a 40 W diode-laser array.

It has, until recently, been widely assumed that interaction with paramagnetic impurities is largely responsible for ^3He wall relaxation at glass surfaces (38, 39). While a reasonable hypothesis, it has never been explicitly demonstrated experimentally. Curiously, attempts to scale up some

successful empirically derived fabrication techniques for small sealed cells to large-volume valved vessels have yielded inconsistent results. This is surprising because a smaller surface-to-volume ratio should lead to longer T_1 s for otherwise similar surfaces. One hypothesis is that some slow-acting surface chemistry (perhaps with Rb as a participant or catalyst) is involved in decreasing the number of paramagnetic sites. Again, however, there are no consistent data to support any one scenario for wall relaxation. It may be possible to sidestep the entire issue: Hsu, Cates, and co-workers recently showed (38) that certain carefully synthesized and very pure sol-gel coatings applied to the surface of small ($<10\text{ cm}^3$) sealed Pyrex cells render wall relaxation nearly negligible. It remains to be seen whether their technique can be applied consistently to larger valved cells.

Pyrex Revisited

Pyrex glass (Corning 7740) is desirable for HP-gas applications because it is inexpensive, ubiquitous, and easy for any glassblower to work. However, there has been general difficulty in achieving consistently long T_1 s in Pyrex cells, and early work in the field suggested that the relatively high permeability of Pyrex to helium leads to strong wall relaxation (40). Pyrex has thus been largely abandoned in favor of more exotic glasses—aluminosilicates such as Corning 1720 and GE 180 from General Electric (41, 42), or borosilicates with smaller helium permeability (43). Despite much trial and error, there is still no foolproof recipe in the literature. In addition, these alternate glasses are expensive, and more difficult to obtain and to work than Pyrex. Of the many tens of Pyrex cells our research groups have made using the same basic techniques, a few have suitably long and stable T_1 s. These cells have no special surface coating, and we have refilled and reused them more than 50 times for MRI experiments. We thus consider still open the question of the utility of Pyrex cells for $\text{HP-}^3\text{He}$.

Recently, in conjunction with the use of a new oil-free vacuum system (see below) and with our identification of a relaxation mechanism involving ferromagnetic sites at or near the surface (44), we have had more consistent success obtaining long T_1 s (40–60 h) in uncoated Pyrex cells. Ferromagnetism in Pyrex cell walls has been confirmed with the observation of T_1 hysteresis, whereby a severe decrease (factors of 2–20) in the relaxation lifetime of cells is caused solely by brief exposure to

a large magnetic field ($\sim 1\text{ T}$). The cells can then be “degaussed” to their original T_1 value by physically rotating them in the presence of a slowly decreasing magnetic field. Details of this unexpected phenomenon will be discussed in a forthcoming publication (44).

Measuring T_1

The T_1 s discussed here are measured relaxation times corresponding to a sum of bulk, gradient-induced, and wall relaxation rates. Measurements are usually made at the $\approx 30\text{ G}$ field relevant for optical pumping using the 100 kHz NMR detection (see below). An FID is generated with a constant low-flip-angle pulse at several appropriately spaced timepoints. The initial height of the FID is then fit to an exponential decay to extract T_1 . It is important to ensure that the flip angle is low enough (and/or a sufficiently small fraction of the sample is excited, as with a surface coil) that magnetization losses generated by the rf pulse are negligible.

Cell Design

A typical cell is shown schematically in Fig. 4. All glass is Pyrex. The main sausage-shaped chamber through which the laser light passes is $40\text{--}50\text{ cm}^3$. The chamber is blown from 25 mm diameter medium wall (4 mm thick) tubing to a diameter of about 38 mm to create a freshly annealed interior surface with a $\approx 2\text{ mm}$ wall thickness. The diameter and wall thickness are sufficient for the desired 10 atm filling pressure. The end windows are rounded for strength. Since laser light passes through the long axis of the main chamber, flat end windows would be better for uniform illumination but may not hold the pressure. The glass blower is instructed to minimize thickening at the very ends of the rounded windows to avoid lensing the laser light. A capillary tube (10 cm long, 1 mm diam.) connects the main chamber to a glass valve (45). The valve has ethylene-propylene o-rings, which are alkali-metal resistant. The capillary serves both to keep the valve and o-rings away from the oven during optical pumping and to isolate the potentially relaxing valve materials from the rest of the cell. Opposite the capillary and also extending from the main chamber is a 6 mm diameter measurement tube, 4 cm long, which is used to monitor and measure the ^3He polarization (see below).

Cell Baking and Rb Distillation

Cells are initially fabricated two at a time by a glass blower, who also attaches them at a right angle to a 0.5 inch diameter glass tube manifold with a retort for the Rb ampule at one end. The other end of the tube is connected to a high-vacuum system. Baking the manifold under vacuum is a crucial (if controversial) step in cell fabrication. It is generally agreed that air and water must be removed, both to prevent reaction with the Rb and especially to prevent rapid ^3He relaxation via collisions with paramagnetic oxygen (46). Baking may also remove other impurities and is generally meant to provide as pristine a surface as possible prior to the introduction of Rb. Most of the lore of cell making has to do with the nature of the vacuum system (pump, valves, and seals), with the length and temperature of the bakeout, and with methods for Rb distillation. We have employed two separate vacuum systems: (1) an oil diffusion pump with a liquid-nitrogen trap, which reaches a base pressure of about 2×10^{-7} Torr and (2) an oil-free turbomolecular drag pump station, which reaches a base pressure of about 2×10^{-8} Torr. The latter system is all stainless-steel with metal-gasketed seals and packless, bellows-sealed valves (47). Good cells for MRI have been made with both systems. The latter system (constructed within the last year) appears to produce cells with $T_1 > 30$ h more consistently. Overall, the evidence for the benefits of the more expensive features in the latter system is suggestive but not conclusive.

Our methods for baking and Rb distillation most closely parallel those of Middleton (48), who gives one of the more complete descriptions of ^3He cell making, albeit using Corning 1720 glass. A 1 g Rb ampule is opened and placed in the retort, after which the entire manifold is sealed and evacuated. The cells and 0.5 inch tube (except for the last few inches and the retort) are wrapped with heater tape and Al foil, and baked under vacuum at 400°C for about two days. During the bake, the Rb metal (m.p. 39°C) is distilled by heating it with a flame and chasing it up the vertical retort to a small reservoir in the 0.5 inch tube next to the retort. The retort is then flame-sealed away from the manifold. After the bake, about 100–300 mg of Rb is further distilled into each cell. The cells, still under vacuum but containing Rb, are finally flame-sealed away from the manifold. In theory, any visible macroscopic amount of Rb should be sufficient to establish a saturated

vapor pressure under optical pumping conditions. The large amount of Rb we use in each cell stems from our empirical finding (corroborated by others) that very small (~ 1 mg or less) amounts of Rb lead to problems attaining the proper density for optical pumping and to fast wall relaxation. Again, we suspect but have no firm evidence of chemical interaction of Rb with the walls, which could affect the vapor-pressure curve.

Refilling System

We use an entirely separate vacuum and gas-handling system to fill and refill cells with the appropriate ^3He - N_2 mixture. We find that once a cell has been evacuated, baked and sealed off, its wall relaxation properties have mostly been determined (provided there is no subsequent catastrophic exposure to the atmosphere), and T_1 remains fairly stable with respect to refilling. The entire refilling system is affixed to aluminum panels mounted vertically on a relay rack. The construction is all stainless steel, with 0.25 inch OD tubing connected with weld fittings, swage fittings, and packed nonrotating stem valves (49). The manifold has an upper gas-filling path having inlets at two points to a lower vacuum manifold. To inhibit oil backstreaming, the vacuum manifold is connected through a u-tube liquid-nitrogen trap and a maize trap (50) to a rotating-vane mechanical pump. The vacuum manifold pressure is monitored with a thermocouple vacuum gauge.

The gas-filling path starts with the lecture bottle containing 25 STP liters (when full) of pre-mixed research-grade ^3He (99%) and N_2 (1%) (51). A small charging volume allows the gas to be dispensed in small quantities. A N_2 and noble-gas purifier (52) follows into a thin 0.030 inch ID stainless steel capillary tube. The capillary tube provides stress relief for the connection to the cell with low dead volume. A tee-connection in the capillary tube connects it both to the cell through the side arm and to a valved one-way vent. This setup allows the entire fill path to be evacuated and purged with clean N_2 gas several times after the cell is connected and before it is refilled. A pressure gauge in the filling path monitors the cell pressure as it is increased to the desired 8–10 atm by admitting 5–10 charges from the bottle.

POLARIZATION MEASUREMENTS

NMR detection at 100 kHz in the 30 Gauss field is the most important tool for monitoring the

polarization process. The hyperpolarization is so large that good signals are obtained with small tip-angle pulses and de-tuned NMR coils. Our low-frequency spectrometer for both ^3He and ^{129}Xe uses traditional operational amplifiers with crystal frequency control in a homodyne configuration (53). We have improved the original design by synchronizing the rising-edge of the pulse timing generator with the 100 kHz clock (54). This ensures consistent flip-angles, even for pulses of only one or a few rf cycles. The spectrometer parts cost about \$600; a measure of the simplicity is that it contains only 25 integrated circuit chips (mostly TTL and op-amps).

The spin polarization is determined from the initial FID amplitude, extrapolated to zero time. In our Helmholtz coil, T_2^* is about 20 ms or more, so that the 1 ms recovery time is inconsequential. With the solenoidal rf coil located on the measurement tube of the cell, the calibration constant relating absolute polarization to signal amplitude is extremely stable. Thus, the measurements in the polarizing field are very good secondary determinations of polarization.

The primary measurement of polarization is performed in high field, comparing the polarized gas signal to the Boltzmann-equilibrium signal of water, benzene, or glycerol. At the 30 Gauss polarizing field, the Boltzmann proton signal would be difficult to detect. We use a very low-Q (resistively damped) probe to avoid radiation damping and tuning drifts and to generate small flip-angle (2° – 3°) pulses with reasonable pulse widths (1 μs or more). The FID amplitudes are compared under the identical conditions of NMR frequency (64.78 MHz, 2.0 T for ^3He , and 1.5 T for protons), pulse length and amplitude, and receiver gain (except for accurate step attenuation). The signals S are proportional to the spin polarizations, spin densities n , and the square of the magnetogyric ratios γ (one factor of γ for the magnetic moment of each spin and one for the flip angle for a given rf pulse in the limit $\sin \theta = \theta$). Thus the absolute polarization P_3 of the ^3He is

$$P_3 = P_1 \left(\frac{\gamma_1}{\gamma_3} \right)^2 \frac{n_1 S_3}{n_3 S_1} \quad [7]$$

where subscripts 3 and 1 refer to ^3He and ^1H (53).

TRANSPORTATION AND DELIVERY

The polarized gas can be moved from the polarizing field into the earth's field and down the

hallway into a high-field electromagnet, for example, all without significant magnetization loss. At all reasonable speeds the spin magnetization follows adiabatically the changing magnetic field direction. We recall the adiabatic criterion that the magnetic field direction must rotate much more slowly than the spins precess about the field (13). In our case the gas must be transported 5 km from the polarizer in the physics laboratory to the medical campus and MR imager without significant T_1 losses. The spins are carried in a 30 Gauss holding field, because of the longer T_1 than in the earth's 0.5 Gauss field. The spin transporter is a solenoid of 10 cm diameter and 50 cm length, powered by a 12 V lead-acid gel battery. The 2.5 h battery lifetime is extended by diodes providing automatic switchover to the 14 V electrical system of an automobile. A coil-form of aluminum tubing also serves as a shield against fluctuating magnetic fields. The weight of the system, solenoid and battery, is about 3.5 kg.

While moving hyperpolarized gas around the laboratory without significant losses in magnetization is routine, we did encounter a particularly surprising and effective source of spin depolarization. The 60 Hz three-phase power transformer in our 10 kW electromagnet power supply produces a large fringe field with high harmonic content. Whenever the polarized gas was carried within 0.5 m of the supply, nearly all of the magnetization was destroyed in just a few seconds by some high harmonic near the ^3He precession frequency (1600 Hz at the earth's field of 0.5 Gauss). Transport through the earth's field is thus particularly dangerous, since the ac power-line fields are concentrated at low frequencies. Solutions to this problem include keeping the spins away from such fields and transportation in the 30 Gauss solenoid, due to the higher precession frequency and the shielding by the aluminum coil-form.

Near the imaging magnet (a 1.5 T, whole-body imager) we store the gas either in a small Helmholtz pair or in the fringe field of the imager (10–60 G). While diffusion through a magnetic field gradient can cause losses in polarization (see above) (5, 33), both the measured magnetization decay and the decay calculated from the measured field gradients near the imager are negligible over typical storage times of approximately one hour.

Delivery of gas to the patient is most convenient at atmospheric pressure; we release the gas from the glass polarizing vessel at 10 atm into a flexible polyethylene bag. We note that in the presence of only 0.01 atm partial pressure

of oxygen, the T_1 of ^3He is already reduced to 3.5 min (46). Thus, the glass cell and flexible bag are attached to a valve assembly and all oxygen is removed by alternating vacuum and nitrogen purge gas. The valve manifold is an all-plastic design to avoid depolarizing surfaces. We mix the 0.5 L bolus of ^3He with 1–2.5 L of N_2 (according to the subject's vital capacity) to provide a full inspiration. Just prior to imaging, the subject begins breathing through a flexible tube of 2 cm diameter and 40 cm length; the ^3He bag is attached and the subject inhales the gas mixture. We have employed various protocols: imaging at full breathhold as well as imaging during initial inspiration, rebreathing with the flexible bag, and subsequent washout. Verbal commands are used to synchronize the subject's breathing and the initiation of MR imaging. At present the moderate cost of ^3He (\approx \$125/liter) does not necessitate gas recovery.

IMAGING HARDWARE

Our ^3He imaging experiments are performed on a 1.5 T Siemens Vision whole body imager with multinuclear capability (63.6 MHz proton, 48.5 MHz ^3He). If the available imager only supports the proton frequency, one can use an external heterodyne approach (55). One shifts the existing, low-level transmitter signal to the ^3He frequency, power amplifies it, and sends it to the duplexer (transmit–receive switch) (56). The preamplified ^3He NMR signal is shifted to the proton frequency and sent to the existing receiver.

For human subjects we use a home-built coil pair with the approximate Helmholtz spacing for both transmit and receive (57). Self-adhesive copper foil of 1.2 cm width is formed into a 30 cm octagon on poster board. Capacitors of 56 pF each are symmetrically located at four corners. A coaxial cable of $3\lambda/4$ electrical length series-feeds each loop. The approximately 25 Ω feed point is transformed (58) by the 50 Ω cable to 100 Ω ; the cables from the two coils are joined by a tee, resulting in a parallel impedance of 50 Ω presented to the imager. Each cable is coiled in two places to form coaxial traps; the traps are approximately parallel-resonant LC circuits to block currents traveling on the outside of the cable braid. Similar traps are used in multiband radio antennas and antenna feeds (58). The effect of loading from a human chest reduces the Q to about 12; hence, no adjustable components are required. The coils are retuned to the proton frequency by

inserting a capacitor at the tee in series with the cable to the imager. While connecting the coils to the imager is in principle as easy as connecting to any NMR spectrometer, we had to obtain proprietary information from the manufacturer to assign a digital name to the coil and to specify the coil as transmit–receive. A wrap-around ^3He chest coil is available (59).

Phantoms are always useful but indispensable when just starting. Because there are no nuclear spins with frequencies near ^3He , there is no substitute for ^3He gas. Our first phantom uses a 50 cm³ glass vessel filled with 8 atm ^3He and 2 atm O_2 to yield a T_1 of about 1 s. A four-turn copper foil coil is wound directly on the glass. For use with the human rf coils, an 8 L fiberglass, valved vessel is filled with 2 atm ^3He and 2 atm O_2 . The large quantity of ^3He , 16 L STP, provides sufficient signal for tune-up and testing, but is expensive (\$2000).

IMAGING STRATEGIES AND RESULTS

It does not overstate the case to say that a different mindset is useful when imaging hyperpolarized ^3He . In traditional MRI, T_1 is regarded as the time for the signal to recover, while the T_1 of hyperpolarized gas is the time for the signal to decay and never return, since the equilibrium polarization is virtually zero by comparison (60). The relaxation rate T_1^{-1} of ^3He in the lungs is linearly proportional to the oxygen concentration, with typical values near 25 s. Evidently the high surface area of the lungs has little effect on T_1 . Indeed, the ^3He T_1 has been used to image the time-dependent oxygen concentration during a breathhold (61). Clearly, hyperpolarized ^3He imaging experiments must be completed rapidly.

Most MRI sequences use many rf pulses to form a single image (1, 2). Since a single 90° pulse would kill the ^3He magnetization, small tip angles must be used with hyperpolarized gases to ration the consumption of magnetization. For studies of time evolution, where the same gas will be imaged repeatedly, even smaller tip angles are required. For a rf pulse of small angle θ , the fraction of remaining longitudinal magnetization is $\cos \theta \cong 1 - \theta^2/2$, where θ is in radians. Hence, a limited number of pulses, equal to $2/\theta^2$, can be used before the magnetization is substantially depleted. In practice, the optimum pulse angle θ is selected by the above criterion; smaller angles will decrease the signal-to-noise (S/N). We note

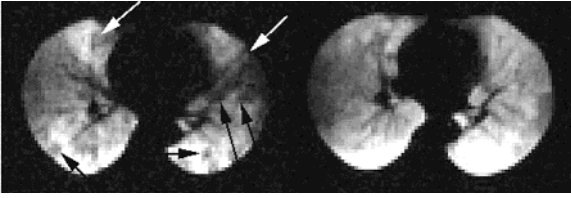


Figure 5 Transverse FLASH images of a patient with asthma, using hyperpolarized ^3He . The same slice is presented before (left) and after (right) administration of a bronchodilator. Several ventilation defects are evident (arrows) but disappear after medication.

that it is never beneficial to signal average from a single bolus of spin magnetization. For example, signal averaging four times requires using a pulse angle half as large, producing half the NMR signal; the $\sqrt{4}$ improvement of S/N by averaging is exactly cancelled by the smaller individual signals. The nonrenewable nature of the magnetization dictates that no automated tune-up sequences (e.g., to find $\pi/2$ pulses) be used. In addition, once the subject has inhaled the hyperpolarized gas, it cannot be repolarized; one gets no second chance.

For high spatial resolution images with ^3He , FLASH (fast, low-angle shots, using gradient-recalled echoes) is widely used (62, 63). The many gas-tissue interfaces in the lung distort the static magnetic field, leading to a short T_2^* of only a millisecond or two for protons in the tissue (64). The ^3He T_2^* at 1.5 T, however, is nearly 20 ms, because the gas occupies approximately spherical regions and because its motion averages over the fields. Echo times TE of 2–10 ms are thus appropriate. We present, in Fig. 5, two-dimensional (2-D) FLASH images for a patient with asthma, before and after the administration of a bronchodilator. The repetition time TR was 7 ms, TE was 3.2 ms, the field of view (FOV) was 225×450 mm, and the 64×128 matrix resulted in square, 3.5 mm pixels. The entire lung was captured as 21 transverse (axial) slices of thickness 10 mm in a total breathhold time of 13 s. An rf pulse of approximately 10° was selected from the considerations above.

A given quantity of polarized gas in animals smaller than humans gives a higher S/N, which can be traded for higher spatial resolution (65). Not only is the ^3He concentration higher, but the rf coils are closer to the lung, on average. The pigs we have imaged have been deeply anesthetized, requiring external ventilation through an endotracheal tube. The flexible bag containing ^3He and N_2 is connected to the endotracheal tube, slowly squeezed by hand, and then valved-off for a

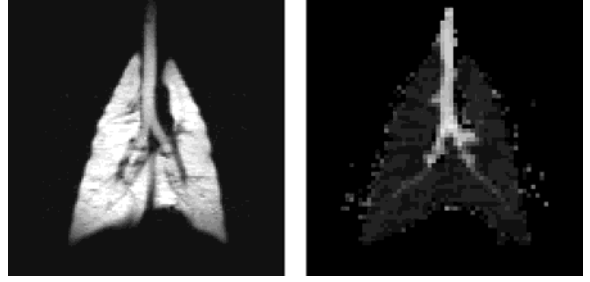


Figure 6 Coronal FLASH image at left of a 23 kg pig's lungs, taken with hyperpolarized ^3He . The trachea and major airways are evident in this slice. At right the diffusivity map is presented. Alveoli restrict the ^3He diffusion, except in the trachea and major airways, where larger diffusivity appears as lighter shades.

breathhold. A typical image from a multi-slice 2-D FLASH sequence is shown in Fig. 6 with square 2 mm pixels and 8 mm slice thickness.

The diffusion of ^3He gas in the lung is substantially reduced by the walls of the alveoli (the smallest lung compartments). Hence, images of the effective diffusivity are particularly sensitive to alveolar wall destruction, which occurs in emphysema (9). Our imaging sequence measures diffusion over approximately 5 ms, during which time the rms displacement of ^3He in free air is about 1.6 mm (using $D = 0.85 \text{ cm}^2/\text{s}$), much greater than the mean alveolar radius of 0.15 mm. Thus, in healthy lung tissue the diffusion of gas atoms will be reduced by repeated collisions with the alveolar walls. Indeed, we find an average effective diffusivity of $0.2 \text{ cm}^2/\text{s}$ in healthy volunteers; in patients with severe emphysema the average diffusivity is near $0.55 \text{ cm}^2/\text{s}$ (9).

We measure the diffusivity on a pixel-by-pixel basis from images taken with and without a diffusion-sensitizing gradient. This gradient waveform is a bipolar pulse (positive, then negative) such as is also used to measure velocities. Two 2-D FLASH sequences (with and without the extra gradient) are interlaced line by line in k-space to minimize the effects of motion. Compared with measuring the apparent diffusivity of biological water, the gas measurement does not require strong gradients and works easily because of the rapid diffusion of the gas. The diffusion attenuates the image taken with the diffusion sensitizing gradient as

$$\frac{M_{\text{with}}}{M_{\text{without}}} = \exp(-bD) \quad [8]$$

with $b = \gamma^2 G^2 t^3 f$, where G is the gradient amplitude, t is the bipolar pulse duration, and f is a

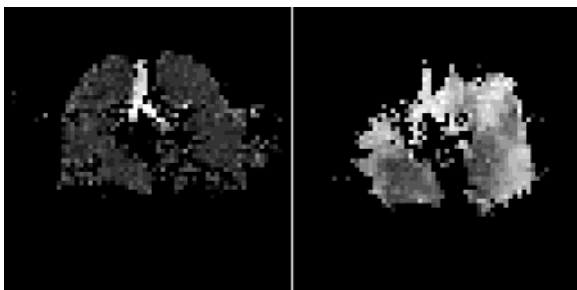


Figure 7 Coronal diffusion maps of a healthy volunteer (left) and a patient with severe emphysema (right). Diffusivity is represented in grayscale, with higher intensity for higher diffusion. At left the trachea is evident from its high diffusion (unrestricted, $0.85\text{ cm}^2/\text{s}$), but the lungs have very low and uniform diffusion ($0.22\text{ cm}^2/\text{s}$). In the emphysema patient, large spatial variation is present, with some regions showing nearly unrestricted diffusion and other areas appearing similar to the healthy lungs.

dimensionless number reflecting the shape of the pulse (trapezoidal ramps, etc.) (66). For each pixel D is calculated from the intensity ratio and the known value of b .

Representative coronal image slices are shown in Fig. 7 for a healthy volunteer (left) and an emphysema patient (right). Here the diffusivity is represented in grayscale, with white being the highest value ($0.85\text{ cm}^2/\text{s}$). At left, the trachea is evident as a stripe of large D , reflecting the absence of alveoli; elsewhere in the healthy lungs the diffusivity is remarkably uniform and small. In the emphysematous lungs at right the diffusion is much larger and has large spatial variations. Some regions of the diseased lung have diffusivity nearly as large as that of the unrestricted diffusion in the trachea. The most diseased portions of the lungs do not receive sufficient gas to permit the ratio-metric determination of D and are represented as black in the figure. A diffusion map for a pig's lungs is also presented in Fig. 6.

Echo-planar imaging (EPI) uses intense gradient waveforms to scan an entire plane of k -space following a single rf excitation pulse (67, 68). Compared to 2-D FLASH imaging where only a single line of k -space is scanned after each rf pulse, EPI offers faster imaging. The larger receiving bandwidth implicit upon rapid scanning leads to larger noise. The use of a single rf pulse allows θ to be larger and results in a larger signal, exactly canceling the larger noise. EPI thus allows images of the same quality to be obtained with the same consumption of magnetization, but faster [8].

In practice, gradient hardware limitations impose a longer value of echo time ($\text{TE} = 12.1\text{ ms}$), leading to larger artifacts resulting from field variations due to susceptibility effects. In particular, the regions of no ^3He signal within major blood vessels have an enlarged appearance.

EPI is especially useful for real-time capture of inhalation and exhalation. Each slice can be imaged in 30 ms, allowing the entire lung to be imaged as 20 transverse slices in 0.6 s. For fewer slices the frame rate can be correspondingly faster. The available S/N is high enough that the same gas can be imaged repeatedly out to 25 s or more, a limit imposed more by T_1 than by rf-consumption of magnetization. Movies can then be created to show full cycles of ventilation, which are particularly useful for determining the spatial distribution of gas that is not exhaled quickly, as is the case for many emphysema patients. Real-time movies of ventilation measured with EPI in healthy and emphysematous lungs may be viewed on the world wide web (69).

SAFETY

Helium is arguably the most inert substance in the universe; this is, of course, equally true of its light isotope ^3He . He-O_2 mixtures are widely used in critical care for their lower density and resulting lower effort of breathing. Heliox mixtures have long been used in deep-sea diving, since the pioneering work of the Navy's Swede Momsen; the narcosis of dissolved nitrogen is avoided by the low solubility of helium. Nevertheless, the US-FDA regards as a drug any imaging substance put in the human body. Our human imaging is performed under an FDA Investigational New Drug exemption. The Rb is of no concern, as the vapor pressure is virtually zero at room temperature (19).

The only known risk of ^3He MR imaging is the lack of oxygen while breathing the $^3\text{He-N}_2$ mixture. To avoid significant and prolonged arterial oxygen desaturation, breathhold times with the anoxic gas mixture are restricted to 10–15 s. The percent oxygen saturation is continuously monitored using an optical finger clip sensor with fiber optic input and output.

CONCLUSIONS

The applications of hyperpolarized gases to NMR and MRI take advantage of the progress in the

atomic physics of optical pumping over the last 40 years. Of crucial importance is the recent development of inexpensive high-power diode laser arrays. Approximately \$25,000 worth of apparatus can allow one to routinely polarize 0.5 L STP quantities of ^3He to polarizations of 40% or more, some 100,000 times larger than equilibrium polarization in ordinary circumstances. In this review we have detailed the physics of optical pumping and spin exchange as well as the necessary hardware, including the all-important diagnostic equipment. Open issues include the development of frequency-narrowed diode lasers for optical pumping and the understanding of wall relaxation mechanisms in polarization cells.

The large ^3He polarization allows high signal-to-noise imaging of gas in human and animal lungs. The nonrenewable nature of the magnetization dictates a unique imaging lifestyle of small-angle pulses, no automatic tune-up sequences, and most of all, after the gas is released, no second chances. Multi-slice 2-D FLASH is a workhorse pulse sequence, yielding high-spatial resolution depictions of the gas-space anatomy. Diffusion imaging is performed with two interleaved FLASH sequences, one with a diffusion-sensitizing gradient. The alveolar walls in healthy lung tissue restrict diffusion and result in a small effective diffusivity. Emphysema in particular destroys alveolar walls, so damaged regions are evident by the higher diffusivity of ^3He . Thus, diffusion maps for emphysema patients reveal the locations of healthy and diseased tissue. High speed echoplanar imaging allows complete image sets of the lung to be repeatedly captured every 0.6 s. This provides a real-time depiction of the motion of gas in and out of the lung; no other technique can measure the spatial distribution of ventilation on a physiologically relevant time scale (less than the 4 s respiratory cycle).

ACKNOWLEDGMENTS

Support from the Whitaker Foundation and the Radiological Society of North America is greatly appreciated. The work at Washington University on small animals was part of the NIH-funded WU Small Animal Imaging Resource. The human work has benefited from the funding and continuing collaboration of J. D. Cooper and the Division of Thoracic Surgery. Jie Zheng is thanked for his participation in the imaging of several pigs. We acknowledge J. J. H. Ackerman's early advice and

assistance. Gifts of imager hours from the Department of Radiology are appreciated. M. Vogel and G. Davis are recognized for helping to schedule patient volunteers from the WU Lung Volume Reduction Surgery program.

REFERENCES

1. Callaghan PT. Principles of nuclear magnetic resonance microscopy. New York: Oxford; 1991.
2. Talagala SL, Lowe IJ. Introduction to magnetic resonance imaging. *Concepts Magn Reson* 1991;3:145–159.
3. Bouchiat MA, Carver TR, Varnum CM. Nuclear polarization of ^3He gas induced by optical pumping and dipolar exchange. *Phys Rev Lett* 1960;5:373–375.
4. Schearer LD, Walters GK. Nuclear spin-lattice relaxation in the presence of magnetic-field gradients. *Phys Rev* 1965;139:A1398–1402.
5. Colegrove FD, Schearer LD, Walters GK. Polarization of ^3He gas by optical pumping. *Phys Rev A* 1963;132:2561–2572.
6. Gamblin RL, Carver TR. Polarization and relaxation processes in ^3He gas. *Phys Rev* 1965;138:A946–960.
7. Chupp TE, Wagshul M. Laser optical pumping of high-density Rb in polarized ^3He targets. *Phys Rev A* 1989;40:4447–4454.
8. Saam BT, Yablonskiy DA, Gierada DS, Conradi MS. Rapid imaging of hyperpolarized gas using EPI. *Magn Reson Med* 1999;42:507–514.
9. Saam BT, Yablonskiy DA, Kodibagkar VD, Leawoods JC, Gierada DS, Cooper JD, Lefrak SS, Conradi MS. MR imaging of diffusion of ^3He gas in healthy and diseased lungs. *Magn Reson Med* 2000;44:174–179.
10. Goodson BM. Using injectable carriers of laser-polarized noble gases for enhancing NMR and MRI. *Concepts Magn Reson* 1999;11:203–223.
11. Brunner E. Enhancement of surface and biological magnetic resonance using laser-polarized noble gases. *Concepts Magn Reson* 1999;11:313–335.
12. Song YQ. Spin polarization-induced nuclear Overhauser effect: an application of spin-polarized xenon and helium. *Concepts Magn Reson* 2000;12:6–20.
13. Slichter CP. Principles of magnetic resonance. New York: Springer-Verlag;1990. p. 66, 257, 223.
14. Becker J, et al. Study of mechanical compression of spin-polarized ^3He gas. *Nucl Instrum Meth A* 1994;346:45–51.
15. Gentile TR, et al. Demonstration of a compact compressor for application of metastability-exchange optical pumping of ^3He to human lung imaging. *Magn Reson Med* 2000;43:290–294.

16. Walker TG, Happer W. Spin exchange optical pumping of noble-gas nuclei. *Rev Mod Phys* 1997;69:629–642.
17. Happer W. Spin exchange, past, present and future. *Ann Phys Fr* 1985;10:645–657.
18. Baranga AB, Appelt S, Romalis MV, Erickson CJ, Young AR, Cates GD, Happer W. Polarization of ^3He by spin exchange with optically pumped Rb and K vapors. *Phys Rev Lett* 1998;80:2801–2804.
19. Killian TJ. Thermionic phenomena caused by vapors of rubidium and potassium. *Phys Rev* 1926;27:578–587. This paper uses the old definition of 1bar = 1N/m^2 ; modern usage is 1bar = 10^5N/m^2 .
20. Newbury NR, Barton AS, Cates GD, Happer W, Middleton H. Gaseous ^3He - ^3He magnetic dipolar spin relaxation. *Phys Rev A* 1993;48:4411–4420.
21. Abragam A. The principles of nuclear magnetism. London: Oxford;1961. p. 322.
22. Stoner RE, Rosenberry MA, Wright JT, Oteiza ER, Walsworth RE. Demonstration of a two species noble gas maser. *Phys Rev Lett* 1996;77:3971–3974.
23. Augustine MP, Bush SD, Hahn EL. Noise triggering of radiation damping from the inverted state. *Chem Phys Lett* 2000;322:111–118.
24. Magnetic Imaging Technologies, Inc. is now part of Nycomed Amersham Imaging, Princeton, NJ.
25. Coherent Semiconductor Group, Santa Clara, CA.
26. CVI Laser, Albuquerque, NM.
27. Cummings WJ, Hausser O, Lorenzon W, Swenson DR, Larson B. Optical pumping of Rb vapor using high-power $\text{Ga}_{1-x}\text{Al}_x\text{As}$ diode laser arrays. *Phys Rev A* 1995;51:4842–4851.
28. Nelson I, Chann B, Walker TG. Spin exchange optical pumping using a frequency-narrowed high power diode laser. *Appl Phys Lett* 2000;76:1356–1358.
29. Zenger JN, Lim MJ, Coulter KP, Chupp TE. Polarization of ^{129}Xe with high power external cavity laser diode arrays. *Appl Phys Lett* 2000;76:1798–1800.
30. Chann B, Nelson I, Walker TG. Frequency-narrowed external-cavity diode-laser-array bar. *Opt Lett* 2000;25:1352–1354.
31. Affinity Industries, Ossipee, NH.
32. Saam BT, Conradi MS. Protection circuitry for high power diode laser arrays. *Rev Sci Instrum* 1998;69:2230–2232.
33. Cates GD, Schaefer SR, Happer W. Relaxation of spins due to field inhomogeneities in gaseous samples at low magnetic fields and at low pressures. *Phys Rev A* 1988;37:2877–2885.
34. Unidata, Orlando, FL.
35. Ocean Optics, Dunedin, FL.
36. Kentek, Pittsfield, NH.
37. Lase-R Shield, Albuquerque, NM.
38. Hsu MF, Cates GD, Kominis I, Aksay IA, Dabbs DM. Sol-gel coated glass cells for spin-exchange polarized ^3He . *Appl Phys Lett* 2000;77: 2069–2071.
39. Timsit RS, Daniels JM, May AD. Nuclear relaxation of ^3He gas on various solid surfaces. *Can J Phys* 1971;49:560–575.
40. Fitzsimmons WA, Tankersley LL, Walkers GK. Nature of surface-induced nuclear-spin relaxation. *Phys Rev* 1969;179:156–165.
41. Chupp TE, Wagshul ME, Coulter KP, McDonald AB, Happer W. Polarized, high-density, gaseous ^3He targets. *Phys Rev C* 1987;36:2244–2251.
42. Jones GL, Gentile TR, Thompson AK, Chowdhuri Z, Dewey MS, Snow WM, Weitfeldt FE. Test of ^3He -based neutron polarizers at NIST. *Nucl Instrum Meth Phys Res A* 2000;440:772–776.
43. Smith TB, Chupp TE, Coulter KP, Welsh RC. Recent advances in spin-exchange pumped polarized ^3He target technology. *Nucl Instrum Meth A* 1998;402:247–249.
44. Jacob RE, Morgan SW, Saam BT, Leawoods JC. ^3He spin relaxation at glass surfaces. In preparation.
45. Kimble/Kontes, Vineland, NJ.
46. Saam BT, Happer W, Middleton H. Nuclear relaxation of ^3He in the presence of O_2 . *Phys Rev A* 1995;52:862–865.
47. Cajon SS-BK4, Macedonia, OH
48. Middleton HL. The spin structure of the neutron determined using a polarized ^3He target. PhD thesis; Princeton University, 1994.
49. Whitey SS-14DK-S4, Highland Heights, OH.
50. Kurt J. Lesker Co., Clairton, PA.
51. Spectra Gases, Branchburg, NJ.
52. UltraPure Systems, Colorado Springs, CO.
53. Saam BT, Conradi MS. Low frequency NMR polarimeter for hyperpolarized gases. *J Magn Reson* 1998;134:67–71.
54. Available at <http://www.physics.wustl.edu/conradi/hpgases.html>, or contact the authors.
55. Ellett JD, Jr., et al. Advances in magnetic resonance, volume 5. Waugh JS, editor. New York, NY: Academic Press; 1971, pp. 117–176.
56. Fukushima E, Roeder SBW. Experimental pulse NMR: a nuts and bolts approach. Reading, MA: Addison-Wesley; 1981.
57. MacFall JR, et al. Human lung air spaces: potential for MR imaging with hyperpolarized ^3He . *Radiology* 1996;200:553–558.
58. Hutchinson CL, Kleinman JP, eds. The ARRL handbook for radio amateurs, 1992 edition. Newington, CT: Amateur Radio Relay League; 1992. p. 20.13.
59. Medical Advances, Milwaukee, WI.
60. Moeller HE, Hedlund LW, Chen XJ, Carey MR, Chawla MS, Wheeler CT, Johnson GA. Measurements of hyperpolarized gas properties in the lung. Part III: ^3He T_1 . *Magn Reson Med* 2001;45:421–430.
61. Deninger AJ, et al. Quantification of regional intrapulmonary oxygen partial pressure evolution during apnea by ^3He MRI. *J Magn Reson* 1999;141:207–216.

62. Elster AD. Gradient-echo MR imaging: techniques and acronyms. *Radiology* 1993;186:1–8.
63. Altes TA, et al. Hyperpolarized ^3He MR lung ventilation imaging in asthmatics: preliminary findings. *J Magn Reson Imaging* 2001;13:378–384.
64. Ailion DC. Application of magnetic resonance to the study of lung. Cutillo AG, ed. Armonk, NY: Futura; 1996.p 33–47.
65. Johnson GA, Cofer GP, Hedlund LW, Maronpot RR, Suddarth SA. Registered ^1H and ^3He magnetic resonance microscopy of the lung. *Magn Reson Med* 2001;45:365–370.
66. Karlicek RF, Lowe IJ. A modified pulse gradient technique for measuring diffusion in the presence of large background gradients. *J Magn Reson* 1980;37:75–91.
67. Mansfield P, Pykett IL. Biological and medical imaging by NMR. *J Magn Reson* 1978;29:355–373.
68. Hennel F. Multiple-shot echo-planar imaging. *Concepts Magn Reson* 1997;9:43–58.
69. Available at <http://www.physics.wustl.edu/conradi/hpgases/epiclip.html>, or contact the authors.

BIOGRAPHY



Jason C. Leawoods received his B.S. degree in physics from Rhodes College in Memphis, Tennessee in 1997; his undergraduate work was on tunable, liquid crystal optical filters and the solar chromosphere. He began graduate studies in 1997

in the Department of Physics at Washington University under the supervision of Professor Mark S. Conradi, where he has researched novel applications of hyperpolarized gases. At Washington University he has focused his research on the application of ^3He MRI to the study of lung diseases such as emphysema and on the transfer of laser-induced polarization to organic molecules through hyperpolarized, supercritical ^{129}Xe . He hopes to continue the work with hyperpolarized gases in the future.



Dmitriy A. Yablonskiy is an Assistant Professor of Radiology and Professor of Physics at Washington University in St. Louis. He obtained his Ph.D. in 1973 from the Institute for Physics and Technology of the Ukrainian Academy

of Sciences. Until 1991 he continued working in the Ukrainian Academy of Sciences on the problems devoted to the theoretical physics of magnetic phenomena in solids. There he published more than 100 papers in peer review scientific journals, a book “Green Functions in the Theory of Magnetism” and was awarded the Ukrainian Prize in the Field of Science and Technology—the highest level prize for physics in Ukraine. After moving to the U.S.A. in 1991, his interests shifted to the field of quantitative magnetic resonance imaging and spectroscopy. He has developed a theoretical model of MR signal formation in biological tissues in the presence of tissue-specific magnetic field inhomogeneities and applied it for *in vivo* quantification of the structure and functioning of blood vessel networks in the brain as well as anisotropic geometrical structures of trabecular bone. Another important direction in Dr. Yablonskiy’s research is the study of human lung physiology by means of MR imaging with hyperpolarized ^3He gas.



Brian Saam has been an assistant professor of physics at the University of Utah since 1999. Originally from Detroit, he completed his undergraduate work at the University of Michigan. He obtained his Ph.D. in 1995 under Will

Happer at Princeton University in the study of hyperpolarized gases, thereafter applying them to MRI of the lung as a post-doctoral fellow under Mark Conradi at Washington University. He holds three U.S. patents in these fields. His research group at Utah continues to study the physics and applications of hyperpolarized gases, including optimal production methods, surface relaxation, NMR in condensed phases of highly polarized ^{129}Xe , and lung imaging of small animals and humans.



David Gierada is an Assistant Professor of Radiology in the Chest Imaging division of the Mallinckrodt Institute of Radiology.



Mark Conradi was educated in magnetic resonance in his undergraduate and graduate years at Washington University, under R. E. Norberg. After postdoctoral study in ESR of free radicals at Oak Ridge National Laboratory under Ralph Livingston, he took an assistant pro-

fessorship at the College of William and Mary. Back at Washington University since 1986, his group is involved in the study of hydrogen atom motions and site occupancies in metal-hydrides and -deuterides. The group is also using hyperpolarized gases for lung imaging in humans and animals. Sensitivity enhancement of analytical NMR is being pursued through polarization transfer from hyperpolarized spins.